

Morphological characterization of shocked porous material

Aiguo Xu, Guangcai Zhang, X. F. Pan, Ping Zhang, and
Jianshi Zhu

National Key Laboratory of Computational Physics,
Institute of Applied Physics and Computational Mathematics, P. O. Box 8009-26,
Beijing 100088, P.R.China

E-mail: Xu_Aiguo@iapcm.ac.cn

Abstract. Morphological measures are introduced to probe the complex procedure of shock wave reaction on porous material. They characterize the geometry and topology of the pixelized map of a state variable like the temperature. Relevance of them to thermodynamical properties of material is revealed and various experimental conditions are simulated. Numerical results indicate that, the shock wave reaction results in a complicated sequence of compressions and rarefactions in porous material. The increasing rate of the total fractional white area A roughly gives the velocity D of a compressive-wave-series. When a velocity D is mentioned, the corresponding threshold contour-level of the state variable, like the temperature, should also be stated. When the threshold contour-level increases, D becomes smaller. The area A increases parabolically with time t during the initial period. The $A(t)$ curve goes back to be linear in the following three cases: (i) when the porosity δ approaches 1, (ii) when the initial shock becomes stronger, (iii) when the contour-level approaches the minimum value of the state variable. The area with high-temperature may continue to increase even after the early compressive-waves have arrived at the downstream free surface and some rarefactive-waves have come back into the target body. In the case of energetic material needing a higher temperature for initiation, a higher porosity is preferred and the material may be initiated after the precursory compressive-waves have scanned all the target body. One may desire the fabrication of a porous body and choose appropriate shock strength according to what needed is scattered or connected hot-spots. With the Minkowski measures, the dependence on experimental conditions is reflected simply by a few coefficients. They may be used as order parameters to classify the maps of physical variables in a similar way like thermodynamic phase transitions.

Submitted to: *J. Phys. D: Appl. Phys.*

1. Introduction

A porous material contains voids or tunnels of different shapes and sizes. Such materials are commonly found in nature and as industrial materials such as wood, carbon, foams, ceramics, bricks, metals and explosives. They have also been used in surgical implant design to fabricate devices to replace or augment soft and hard tissues, etc. In order to use them effectively, their mechanical and thermodynamical properties must be understood in relation to their mesoscopic structures [1, 2].

In this work we focus on porous materials under shock wave reaction. When a porous material is shocked, the cavities inside the sample may result in jets and influence its back velocity [3]. Cavity nucleation due to tension waves controls the spallation behavior of the material [4]. Cavity collapse plays a prominent role in the initiation of energetic reactions in explosives [5]. In this side, most of previous studies concerned the Hugoniot [6–13] and the equation of state [14–16]. It is known that, under strong shocks, the porous material is globally in a nonequilibrium state and show complex dissipative structures. How to describe and pick up information from such a system is still an open problem. In this work we introduce the Minkowski functionals to measure the morphological behaviors of the map of state variable and use them to probe the procedure of shock wave reaction on porous material.

This study needs also a powerful simulation tool. The molecular dynamics can discover some atomistic mechanisms of shock-induced void collapse [17, 18], but the spatial and temporal scales it may cover are far from those comparable with experiments. To overcome this scale limitation, we resort to a newly developed mesoscopic particle method, the material-point method (MPM) [19–24]. The MPM was originally introduced in fluid dynamics by Harlow, et al [19] and extended to solid mechanics by Burgess, et al [20], then developed by various researchers, including us [25–27]. The other reason for using the MPM is related to the severe difficulties of the traditional Eulerian and Lagrangian methods in treating with shocked porous materials. The material under investigation is generally highly distorted during the collapsing of cavities. The Eulerian description is not convenient for tracking interfaces. When the Lagrangian formulation is used, the original element mesh becomes distorted so significantly that the mesh has to be re-zoned to restore proper shapes of elements. The state fields of mass density, velocities and stresses must be mapped from the distorted mesh to the newly generated one. This mapping procedure is not a straightforward task, and introduces errors. The MPM not only takes advantages of both the Lagrangian and Eulerian algorithms but makes it possible to avoid their drawbacks as well. At each time step, calculations consist of two parts: a Lagrangian part and a convective one. Firstly, the computational mesh deforms with the body, and is used to determine the strain increment, and the stresses in the sequel. Then, the new position of the computational mesh is chosen (particularly, it may be the previous one), and the velocity field is mapped from the particles to the mesh nodes. Nodal velocities are determined using the equivalence of momentum calculated for the particles and for the computational grid.

The following part of the paper is planned as follows. Section 2 briefly reviews the Minkowski descriptions. Section 3 presents the theoretical model of the material under consideration. Simulation results are shown and analyzed in section 4. Section 5 makes the conclusion.

2. Brief review of morphological characterization

A variety of techniques can be used to describe the complex spatial distribution and time evolution of state variables in the shocked porous material. In this study we concentrate on the set of statistics known as Minkowski functionals [28]. A general theorem of integral geometry states that all properties of a d -dimensional convex set (or more generally, a finite union of convex sets) which satisfy translational invariance and additivity (called morphological properties) are contained in $d + 1$ numerical values [29]. For a pixelized map $\psi(\mathbf{x})$, we consider the excursion sets of the map, defined as the set of all map pixels with value of ψ greater than some threshold ψ_{th} (see, e.g., Refs. [30, 31]), where \mathbf{x} is the position, ψ can be a state variable like temperature T , density ρ or pressure P ; ψ can also be the velocity \mathbf{v} or its components, some specific stress, etc. Then the $d + 1$ functionals of these excursion sets completely describe the morphological properties of the underlying map $\psi(\mathbf{x})$. In the case of two or three dimensions, the Minkowski functionals have intuitive geometric interpretations.

For a two-dimensional map, the three Minkowski functionals correspond geometrically to the total fractional area A of the excursion set, the boundary length L of the excursion set per unit area, and the Euler characteristic χ per unit area (equivalent to the topological genus). Such a description has been successfully used to describe patterns in reaction-diffusion system [32], the cosmic microwave background temperature fluctuations [33], and patterns in phase separation of complex fluids [34–37], etc.

In this work we probe the shocked porous material via checking the temperature map $T(\mathbf{x}, t)$, where the time t is explicitly denoted. The maps of other physical variables can be analyzed in a similar way. When the temperature $T(\mathbf{x})$ is beyond the threshold value T_{th} , the grid node at position \mathbf{x} is regarded as a white (or hot) vertex, else it is regarded as a black (or cold) one. For the square lattice, a pixel possesses four vertices. A region with connected white (hot) or black (cold) pixels is defined as a white (hot) or black (cold) domain. Two neighboring white and black domains present a clear interface or boundary. When we increase the threshold contour-level T_{th} from the lowest temperature to the highest one in the system, the white area A will decrease from 1 to 0; the boundary length L first increases from 0, then arrives at a maximum value, finally decreases to 0 again. There are several ways to define the Euler characteristic χ . Two simplest ones are

$$\chi = N_W - N_B, \tag{1}$$

Figure 1. (in JPG format) Configurations with temperature contours. $\delta = 2$ and $v_{init} = 1000\text{m/s}$. From left to right, $t=500\text{ns}$, 1500ns , 2000ns , and 2500ns , respectively. The length unit here is $10\ \mu\text{m}$.

or

$$\chi = \frac{N_W - N_B}{N}, \quad (2)$$

where N_W (N_B) is the number of connected white (black) domains, N is the total number of pixels. The only difference of the two definitions is that the first keeps χ an integer. In contrast to the white area A and boundary length L , the Euler characteristic χ describes the connectivity of the domains in the lattice. It describes the pattern in a purely topological way, i.e., without referring to any kind of metric. It is negative (positive) if many disconnected black (white) regions dominate the image. A vanishing Euler characteristic indicates a highly connected structure with equal amount of black and white domains. Specifically, for the definition (1), the integer χ equals -1 when one has a black drop in a large white lattice, and $+1$ vice versa, since the surrounding white (black) region does conventionally not count. In this paper, we use the second definition without making any ambiguity. The ratio

$$\kappa = \frac{N_W - N_B}{NL} \quad (3)$$

describes the mean curvature of the boundary line separating black and white domains. Despite having global meaning, the Euler characteristic χ can be calculated in a local way using the additivity relation [32].

3. Theoretical model of the material

In this study the material is assumed to follow an associative von Mises plasticity model with linear kinematic and isotropic hardening [38]. Introducing a linear isotropic elastic relation, the volumetric plastic strain is zero, leading to a deviatoric-volumetric decoupling. So, it is convenient to split the stress and strain tensors, $\boldsymbol{\sigma}$ and $\boldsymbol{\varepsilon}$, as

$$\boldsymbol{\sigma} = \mathbf{s} - P\mathbf{I}, P = -\frac{1}{3}\text{Tr}(\boldsymbol{\sigma}), \quad (4)$$

$$\boldsymbol{\varepsilon} = \mathbf{e} + \frac{1}{3}\theta\mathbf{I}, \theta = \frac{1}{3}\text{Tr}(\boldsymbol{\varepsilon}), \quad (5)$$

where P is the pressure scalar, \mathbf{s} the deviatoric stress tensor, and \mathbf{e} the deviatoric strain. The strain \mathbf{e} is generally decomposed as $\mathbf{e} = \mathbf{e}^e + \mathbf{e}^p$, where \mathbf{e}^e and \mathbf{e}^p are the traceless elastic and plastic components, respectively. The material shows a linear elastic response until the von Mises yield criterion,

$$\sqrt{\frac{3}{2}} \|\mathbf{s}\| = \sigma_Y, \quad (6)$$

is reached, where σ_Y is the plastic yield stress. The yield σ_Y increases linearly with the second invariant of the plastic strain tensor \mathbf{e}^p , i.e.,

$$\sigma_Y = \sigma_{Y0} + E_{\text{tan}} \|\mathbf{e}^p\|, \quad (7)$$

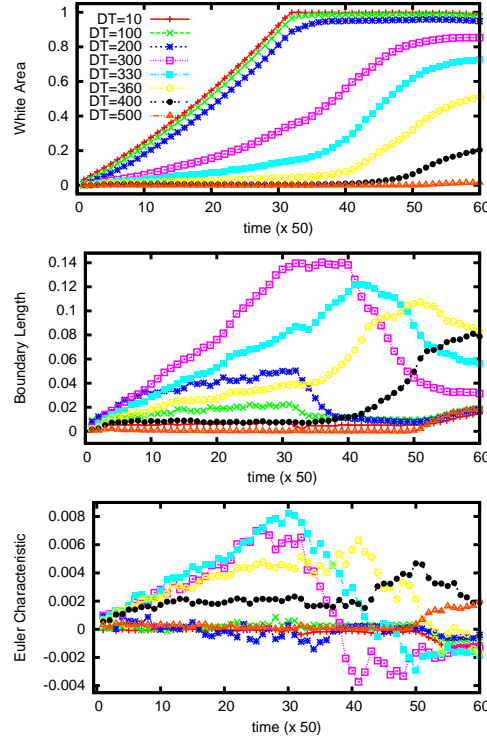


Figure 2. (Color online) Minkowski measures for the procedure shown in Fig.1. The contour levels of the temperature increment are shown in the legend.

where σ_{Y0} is the initial yield stress and E_{tan} the tangential module. The deviatoric stress \mathbf{s} is calculated by

$$\mathbf{s} = \frac{E}{1 + \nu} \mathbf{e}^e, \quad (8)$$

where E is the Yang's module and ν the Poisson's ratio. Denote the initial material density and sound speed by ρ_0 and c_0 , respectively. The shock speed U_s and the particle speed U_p after the shock follows a linear relation, $U_s = c_0 + \lambda U_p$, where λ is a characteristic coefficient of material. The pressure P is calculated by using the Mie-Grüneissen state of equation which can be written as

$$P - P_H = \frac{\gamma(V)}{V} [E - E_H(V_H)] \quad (9)$$

In Eq.(9), P_H , V_H and E_H are pressure, specific volume and energy on the Rankine-Hugoniot curve, respectively. The relation between P_H and V_H can be estimated by experiment and can be written as

$$P_H = \begin{cases} \frac{\rho_0 c_0^2 (1 - \frac{V_H}{V_0})}{(\lambda - 1)^2 (\frac{\lambda}{\lambda - 1} \times \frac{V_H}{V_0} - 1)^2}, & V_H \leq V_0 \\ \rho_0 c_0^2 (\frac{V_H}{V_0} - 1), & V_H > V_0 \end{cases} \quad (10)$$

In this paper, the transformation of specific internal energy $E - E_H(V_H)$ is taken as the plastic energy. Both the shock compression and the plastic work cause the increasing of

Figure 3. (in JPG format) Configurations with temperature contours. $\delta = 1.4$ and $v_{init} = 1000\text{m/s}$. From left to right, $t=500\text{ns}$, 1100ns , 1400ns , and 1700ns , respectively. The length unit here is $10\ \mu\text{m}$.

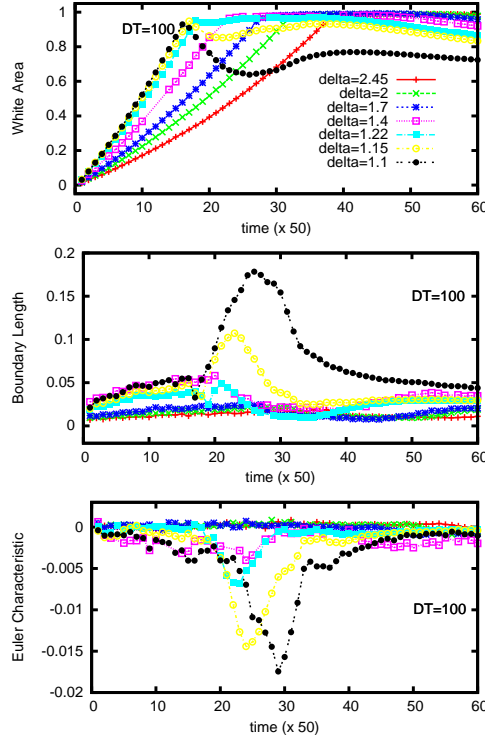


Figure 4. (Color online) Minkowski measures for cases with various porosities. $T_{th} = 400\text{K}$. The values of porosity are shown in the legend.

temperature. The increasing of temperature from shock compression can be calculated as:

$$\frac{dT_H}{dV_H} = \frac{c_0^2 \cdot \lambda (V_0 - V_H)^2}{c_v [(\lambda - 1)V_0 - \lambda V_H]^3} - \frac{\gamma(V)}{V_H} T_H. \quad (11)$$

where c_v is the specific heat. Eq.(11) can be derived from thermal equation and the Mie-Grüneisen state of equation [39]. The increasing of temperature from plastic work can be calculated as:

$$dT_p = \frac{dW_p}{c_v} \quad (12)$$

Both the Eq.(11) and the Eq.(12) can be written as the form of increment.

In this paper we choose aluminum as the sample material. The corresponding parameters are $\rho_0 = 2700\ \text{kg/m}^3$, $E = 69\ \text{Mpa}$, $\nu = 0.33$, $\sigma_{Y0} = 120\ \text{Mpa}$, $E_{\tan} = 384\ \text{MPa}$, $c_0 = 5.35\ \text{km/s}$, $\lambda = 1.34$, $c_v = 880\ \text{J/(Kg}\cdot\text{K)}$, $k = 237\ \text{W/(m}\cdot\text{K)}$ and $\gamma_0 = 1.96$ when the pressure is below $270\ \text{GPa}$. The initial temperature of the material is $300\ \text{K}$.

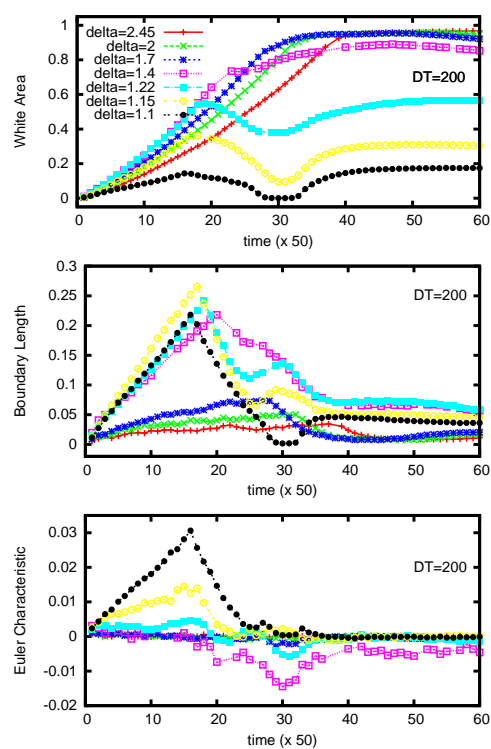


Figure 5. (Color online) Minkowski measures for cases with various porosities. $T_{th}=500\text{K}$. The values of porosity are shown in the legend.

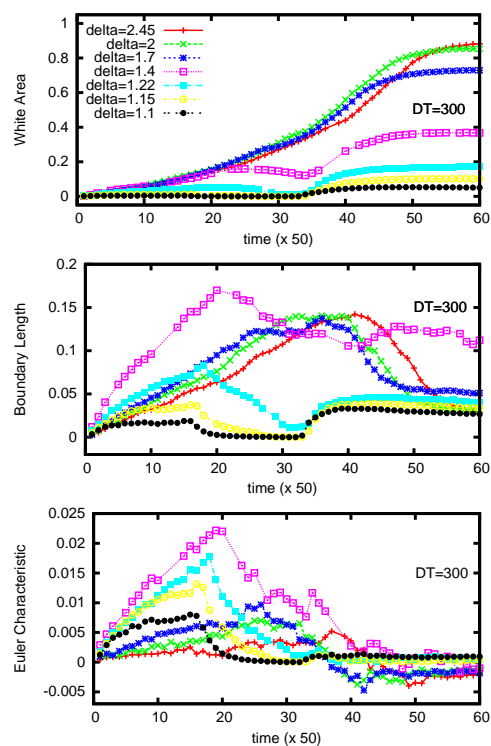


Figure 6. (Color online) Minkowski measures for cases with various porosities. $T_{th}=600\text{K}$. The values of porosity are shown in the legend.

Figure 7. (in JPG format) Configurations with temperature contours. $\delta = 1.4$ and $v_{init} = 500\text{m/s}$. From left to right, $t = 500\text{ ns}$, 1500 ns , 2000 ns , and 2500 ns , respectively. The length unit here is $10\ \mu\text{m}$.

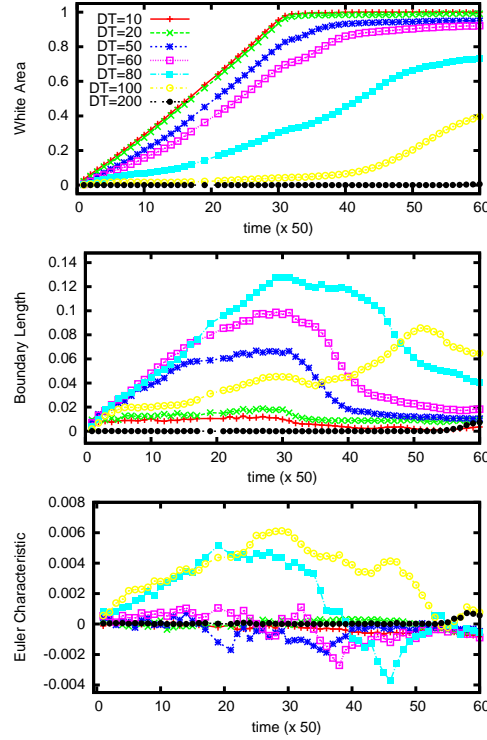


Figure 8. (Color online) Minkowski measures for the case of $\delta = 1.4$ and $v_{init} = 500\text{m/s}$. The values of contour level are shown in the legend.

4. Simulation results and physical interpretation

In our numerical experiments the porous material is fabricated by a solid material body with an amount of voids randomly embedded. We denote the mean density of the porous body as ρ and the density of the solid portion as ρ_0 . The porosity is defined as $\delta = \rho_0/\rho$. The present work concentrates on two-dimensional case and the porosity δ is controlled by the total number N_{void} and mean size r_{void} of voids embedded. The shock wave reacting on the target porous body is loaded via a colliding by a rigid wall with the same material. We choose the coordinate system where the rigid wall is horizontal and keeps static at the position $y = 0$, the target porous body is on the upper side of the rigid wall and moves towards the rigid wall at a velocity $-v_{init}$. The porous body begins to touch the rigid wall at the time $t = 0$. The simulated porous body is initially 1 mm in width and 5 mm in height, as shown in Fig. 1. Periodic boundary conditions are set in the horizontal directions, which means the real system under consideration is composed of many of the simulated ones aligned periodically in the horizontal direction.

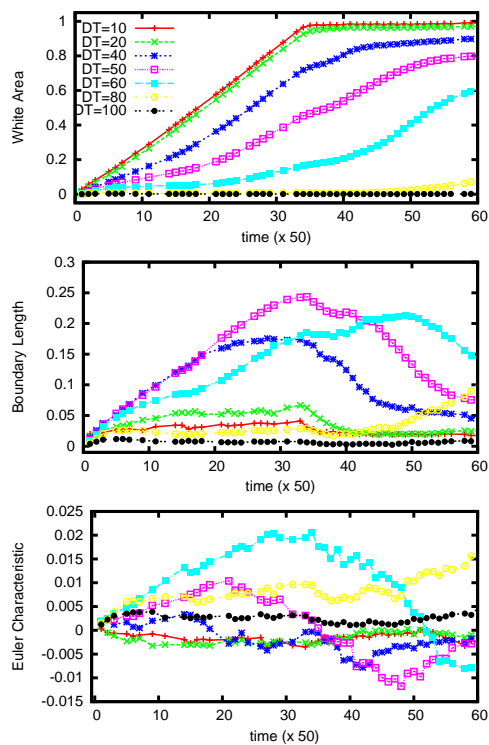


Figure 9. (Color online) Minkowski measures for the case of $\delta = 1.4$ and $v_{init} = 400\text{m/s}$. The values of contour level are shown in the legend.

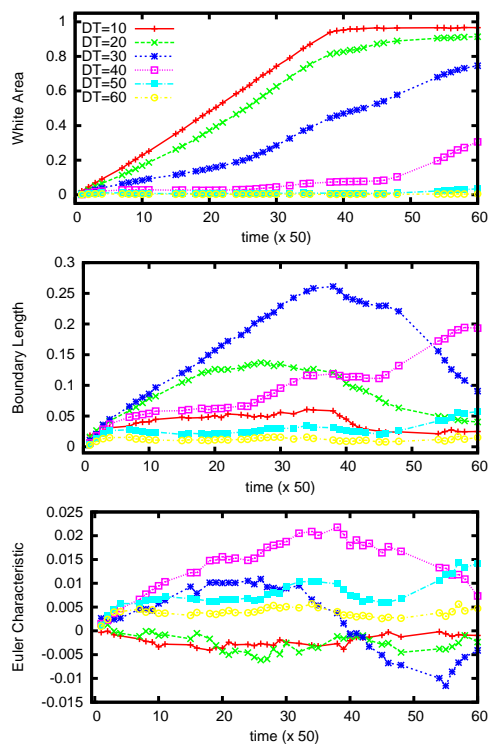


Figure 10. (Color online) Minkowski measures for the case of $\delta = 1.4$ and $v_{init} = 300\text{m/s}$. The values of contour level are shown in the legend.

4.1. Case with $\delta = 2$ and $v_{init} = 1000\text{m/s}$

Figure 1 shows a set of snapshots for a procedure that a shock wave is reacting on a porous body, where the contours denote temperature. From blue to red, the temperature increases. The porosity $\delta = 2$, $v_{init} = 1000\text{m/s}$. The time $t=500\text{ns}$, 1500ns , 2000ns , 2500ns for the four snapshots from left to right. It is clear that, different from the case with uniform material, the original shock wave is scattered and dispersive in the porous body. The first two snapshots show the loading procedure. When $t = 500 \text{ ns}$, the early compressive waves arrive at about $y = 1 \text{ mm}$; when $t = 1500 \text{ ns}$, they arrive at about $y = 3.1 \text{ mm}$. The last two snapshots show the procedure of downloading. When compressive waves arrive at the upper free surface, rarefactive waves are reflected back into the target porous body. Under the tension wave, the height of the porous body increases with time. In fact, before the compressive waves arrive at the upper free surface, a large number of local downloading phenomena have occurred within the porous body. When the initial shock wave or a compressive wave encounters a void, rarefactive waves are reflected back and propagate within the compressed portion, which destroys the original possible equilibrium state there. Since the details of wave series are very complex, when we mention the value of a state variable, for example the density, we refer to its local mean value.

To perform the Minkowski functional analysis for the temperature map, we can choose a threshold temperature T_{th} and pixelize the map into white regions (with $T \geq T_{th}$) and black regions (with $T < T_{th}$). Figure 2 shows the Minkowski measures for the same procedure as in Fig.1. “ DT ” in the legend means $T_{th} - 300$. The unit of temperature is K. The time unit is ns. When DT is very small, the wave front is nearly a plane, which is similar to the case with shock reacting on uniform solid material. When $DT = 10\text{K}$, the total fractional white area A increases up to be nearly 1 at the time $t = 1600 \text{ ns}$ and keeps this value until the time $t = 2600\text{ns}$, then has a slight decreasing. This means the early compressive wave arrives at the upper free surface at about, in fact before, the time $t = 1600 \text{ ns}$, nearly all material particles in the target body have a temperature beyond 310 K during the following 1000ns. In the downloading procedure the rarefactive waves make a very small fraction of material particles decrease their temperature to below 310 K. With the increase of DT , the white area A decreases. For the case with $DT = 100 \text{ K}$, when $t = 1900 \text{ ns}$, the white area arrives at a steady value 0.96, which means 4% of the material particles could not get a temperature higher than 400 K in the whole procedure shown here. Compared with the case of $DT = 10\text{K}$, we can get another piece of information, the temperature increase in shocked portion of porous material is much slower than in shocked uniform solid material. We can find the physical reason for this by considering the void effects in shocked porous body. When the compressive wave arrives at a void, it is decomposed of many components. The components in the solid portion move forwards more quickly, while the portion facing the void may result in jet phenomenon. When jetted material hit the downstream wall of the void, new compressive waves are created. At the same time, the void

reflects rarefactive wave back to the compressed region. A large number of similar processes exist in the shocked porous system. Thus, the shock loading procedure in the porous body is manifested as successive reactions of many compressive and rarefactive waves. In the shock-loading procedure, the compressive waves dominate. Each plastic deformation makes a temperature increment. The curve for the case of $DT = 200$ K can be interpreted in a similar way. When DT increases from 200K to 300K, the curve of white area has a significant variation. For the case of $DT = 400$ K, the white area arrives at 0.2 at the time $t = 3000$ ns, which means 80% of material particles could not get a temperature higher than 700 K up to this time. When $DT = 500$ K, the white area keeps nearly zero during the whole procedure shown here, which means no local temperature is higher than 800K in the system up to the time $t = 3000$ ns. For cases with $DT = 300$ K, 330K, 360K and 400K, after the initial slow increasing period, the white (hot) area has a quick increasing period. The latter indicates that a large amount of “hot-spots” in the previously compressed region coalesced during that period. After that the increasing of A with t shows a slowing-down. The slope of the $A(t)$ curve approximately corresponds to the mean propagation speed of some components of the compressive waves. Therefore, the first Minkowski measure indicates that, in porous material, when a velocity D of the compressive-wave-series mentioned, the corresponding contour-level of a state variable like temperature should also be stated. From this figure, it is clear that $D(T_{th})$ decreases with the increasing of T_{th} ; The total fractional white (hot) area $A(t)$ shows a parabolic behavior during the initial period; When DT approaches 0, $A(t)$ behavior goes back to be linear.

Now we go to the second Minkowski measure, the boundary length L . To understand this measure, we can consider the three-dimensional plot of $T(x, y)$ as a mountain. In the case where the mountain has only one peak, when we increase the contour level T_{th} , the white area A decreases, and the boundary length L decreases, too. But in the case where the mountain has more than one peaks, the situation will not be so simple: the white area A may decrease while the boundary length L increases. For the case of $DT = 10$ K, after the initial increase corresponding to the getting contact of the target body with the rigid wall, the boundary length L keeps a small constant for a long time until about $t = 2600$ ns. The fact that the boundary length L keeps constant while the white area A increase means also that the compressive wave is propagating towards the upper free surface and the wave front is nearly a plane in the pixelized temperature map. The increasing of boundary length L after the time $t = 2600$ ns is accompanying with the decreasing of white area A , which means some small black (cold) spots occur. The curves for $DT = 100$ K and $DT = 200$ K show similar information. They first increase with time due to the appearance of more “hot-spots”, then decreases due to the coalesce of “hot-spot”, finally increase, accompanied by the slight decrease of the total fractional white area A . When $DT = 300$ K, during the period with 1500 ns $< t < 2500$ ns, the white area A increases, while the total fractional boundary length L is nearly a constant. Considering that the wave front has not been a plane any more for this threshold temperature, this result indicates the

following information: during this period, the compressive waves propagate forwards, more scattered “hot-spots” appear in the newly compressed region; at the same time, some previous scattered “hot-spots” coalesce. From 2500ns to 3000ns, the white area A increases very slowly, but the boundary length L decreases quickly. This result show that the increasing of white area A is mainly due to coalesce of previous scattered “hot-spots”. The curves for $DT = 330\text{K}$ and $DT = 360\text{K}$ can be understood in the similar way. For the present shock strength, only very few material particles can get a temperature beyond 700K before the time $t = 2000\text{ns}$. Therefore, the boundary length L for the case with $DT = 400\text{K}$ has a meaningful increase only after $t = 2000\text{ns}$.

When DT is small, $T > T_{th}$ in (nearly) all of the compressed portion and $T < T_{th}$ in the uncompressed part of the material body. The temperature map shows a highly connected structure with (nearly) equal and very small amount of black and white domains. So, the Euler characteristic χ keeps close to zero in the whole shock-loading procedure and the mean curvature κ is nearly zero. The value of χ decreases to be evidently less than zero in the downloading procedure, which indicates that the number of domains with $T < T_{th}$ increases. (See the $\chi(t)$ curves for cases with $DT = 10$, $DT = 100$ and $DT = 200$ in Fig.2.) With the increasing of the contour level T_{th} , more regions changes their color from white ($T > T_{th}$) to black ($T < T_{th}$). The pattern evolution in the shock-loading procedure can be regarded as that scattered white domains appear gradually with time in the black background. So the Euler characteristic χ is positive and increasing with time. (See the $\chi(t)$ curves for cases with $DT = 300$, $DT = 330$ and $DT = 360$ in Fig.2.) When the contour level T_{th} is further increased up to 700K , a meaningful fraction of material particles could not get a temperature higher than the contour level T_{th} . The saturation phenomenon in the χ curve during the period, $550\text{ns} < t < 2100\text{ns}$, indicates that the numbers of connected “hot” and “cold” domains vary with time in a similar way. The increase of χ in the period, $2100\text{ns} < t < 2500\text{ns}$, is due to that the rarefactive waves make mean-temperature decrease, correspondingly, some connected “hot-domains” are disconnected as scattered “hot-spots” again. For the case of $DT = 500\text{K}$, the pixelized temperature map is nearly in black. So, the Euler characterization χ is nearly zero.

4.2. Effects of porosity

Figure 3 shows a set of snapshots for the case with a lower porosity, $\delta = 1.4$. The other conditions are the same as in Fig.1. From left to right, the four configurations correspond to the times, $t = 500\text{ns}$, 1100ns , 1400ns and 1700ns . Compared with the snapshots in Fig.1, it is clear that the propagation velocity of compressive wave increases with the decreasing of porosity. At time $t = 500\text{ns}$, in the system with $\delta = 1.4$, the compressive wave arrives at about $y = 1750\mu\text{m}$; while in the system with $\delta = 2$, the compressive wave only arrives at about $y = 1000\mu\text{m}$. In the case of $\delta = 1.4$, the compressive wave has arrived the top free surface and the rarefactive wave has been reflected back to the target body before the time $t = 1400\text{ns}$; while in the case of $\delta = 2$, the shock-loading

procedure has not been finished up to $t = 1500\text{ns}$.

Figure 4 shows the Minkowski measures for cases with various porosities, where $T_{th} = 400\text{K}$ and the values of porosity, $\delta = 2.45, 2, 1.7, 1.4, 1.22, 1.15, 1.1$ are shown in the legend. In the subfigure for white area A , the initial shock-loading part presents meaningful information: the velocity D of the compressive-wave-series is smaller for a higher porosity δ . The most significant property in the subfigure for boundary length L is that the largest boundary length L_{max} increases as δ decreases. When $\delta = 1.1$, the total boundary length L gets the maximum value at about $t = 1250\text{ns}$. This result indicates that the highest temperature in shocked porous material decreases when the porosity approaches 1. The Euler characteristic χ becomes more negative when the porosity δ decreases from 2.45 to 1.1, which means the disconnected “cold” domains with $T < 400\text{K}$ dominate more the image.

Figures 5 and 6 show the Minkowski measures for the same porosities but higher temperature thresholds, $T_{th} = 500\text{K}$ and $T_{th} = 600\text{K}$. They present supplementary information to Fig. 4. For cases with $\delta = 1.4, 1.22, 1.15$ and 1.1 , only 88%, 55%, 36% and 15% of the material particles get the temperature higher than 500K. For cases with $\delta = 1.4$ and 1.22 , and only 16% and 6% get the temperature higher than 600K in the shock-loading procedure. When $T_{th} = 500\text{K}$, the case with $\delta = 1.15$ has the maximum boundary length and the case with $\delta = 1.1$ has the maximum Euler characteristic. When $T_{th} = 600\text{K}$, the case with $\delta = 1.4$ has the maximum boundary length and maximum Euler characteristic, which means the “hot-spots” with $T > 600\text{K}$ are scatteredly distributed in the “cold” background with $T < 600\text{K}$.

4.3. Effects of initial shock-wave-strength

We now study the effects of different initial impacting speeds. Figure 7 shows a set of snapshots for the case with $\delta = 1.4$ and $v_{init} = 500\text{m/s}$. From left to right, the four configurations are for the times $t = 500\text{ns}, 1500\text{ns}, 2000\text{ns}$ and 2500ns . From the first two, we observe the upward propagation of compressive wave in the target body. From the last two, we observe the downward rarefactive effects. Compared with Fig.3, it is clear that the velocity D of compressive-wave-series and the highest temperature T_{max} decreased. The Minkowski measures for this procedure is shown in Fig. 8. Such a shocking procedure could not produce “hot-spot” with $T = 500\text{K}$. High-temperature “Hot-area” continue to increase even after some precursory compressive waves have scanned all the target body and some rarefactive waves have come into the target body from the upper free surface. Up to the time $t = 3000\text{ns}$, the fractional area of “Hot-spots” with $T > 400\text{K}$ reaches 40%, the fractional area for $T > 380\text{K}$ reaches 74%, that for $T > 360\text{K}$ reaches 91%. The contour-level with $T = 380\text{K}$ has the largest boundary length at about $t = 1500\text{ns}$ when the “hot-spots” mainly distribute scatteredly in the “cold” background. Figures 9 and 10 show the Minkowski measures for cases with the same porosity but lower initial impacting speeds. $v_{init} = 400\text{m/s}$ in Fig.9 and $v_{init} = 300\text{m/s}$ in Fig.10. With the decrease of initial impact speed, the

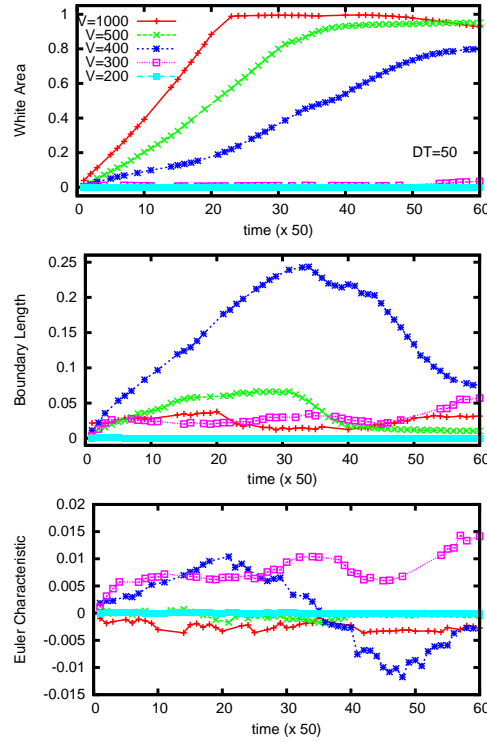


Figure 11. (Color online) Minkowski measures for cases with various shock strengths. $\delta = 1.4$. The values of initial impacting speed v_{init} are shown in the legend.

highest temperature T_{\max} in the system further decreases; the total fractional white area A for low contour-level, for example $DT = 10K$, increases with time in a more linear way.

We compare Minkowski measures for different initial impacting speeds in Fig. 11, where $\delta = 1.4$, $DT = 50K$, $v_{init} = 1000m/s$, $500m/s$, $400m/s$, $300m/s$, and $200m/s$. It is clear that the higher the initial impacting speed, the closer to be linear the $A(t)$ curve. The case of $v_{init} = 400m/s$ has the longest total boundary separating the “hot” and “cold” domains. For this case, disconnected “hot” regions dominate the image from the topology side in the shock-loading procedure; disconnected “cold” regions dominate in the downloading procedure.

5. Conclusions

Under shock wave reaction, the porous material is globally in a nonequilibrium state and shows complex dissipative structures. We pixelize the map of temperature into Turing patterns and introduce morphological measures for it. Relevance of the total fractional white area A , boundary length L and the Euler characteristic χ to the thermodynamical properties of material is revealed. Various experimental conditions are simulated via the material-point method. Numerical results indicate that, the shock wave reaction results in a complicated sequence of compressions and rarefactions in porous material. The increasing rate of A roughly gives the velocity D of a compressive-wave-series. When a

velocity D is mentioned, the corresponding threshold contour-level of the temperature should also be stated. When the threshold contour-level increases, D becomes smaller. The area A increases parabolically with time t during the initial period. The $A(t)$ curve goes back to be linear in the following three cases: (i) when the porosity δ approaches 1, (ii) when the initial shock becomes stronger, (iii) when the contour-level approaches the minimum value of the temperature. The area with high-temperature may continue to increase even after the early compressive-waves have arrived at the downstream free surface and some rarefactive-waves have come back into the target body. In the case of energetic material needing a higher temperature for initiation, a higher porosity is preferred and the material may be initiated after the precursory compressive-waves have scanned all the target body. One may desire the fabrication of a porous body and choose the appropriate shock strength according to what needed is scattered or connected hot-spots. The same measures can also be used to analyze the maps of other physical variables, like the density, velocity, or various stresses. With the Minkowski measures, the dependence on experimental conditions is reflected simply by a few coefficients. They may be used as order parameters to classify the maps of state variable in a similar way like thermodynamic phase transitions.

Acknowledgments

We warmly thank Jianguo Wang, Hua Li, Yangjun Ying for helpful discussions on shock waves and porous material. A.Xu is grateful to Drs. G. Gonnella and A. Lamura for constructive discussions on Minkowski functionals. This work is supported by Science Foundations of LCP and CAEP, national Science Foundation of China (under Grant Nos. 10702010,10775018 and 10604010).

References

- [1] M. Lundberg, B. Skårman, F. Cesar, L. R. Wallenberg, *Microporous and Mesoporous Materials*, **54** 97 (2002).
- [2] G. Lu, G.Q.M. Lu, and Z.M. Xiao, *J. Porous Materials* **6**, 359 (1999).
- [3] D.B.Reisman, W.G.Wolfer, A. Elsholz, and M.D. Furnish, *J. Appl. Phys.* **93**, 8952 (2003).
- [4] E. Dekel, S. Eliezer, Z. Henis, E. Moshe, A. Ludmirsky, and I. B. Goldberg, *J. Appl. Phys.* **84**, 4851 (1998); R. W. Minich, J. U. Cazamias, M. Kumar, and A. J. Schwartz, *Metall. Mater. Trans. A* **35**, 2663 (2004).
- [5] N. K. Bourne, *Shock Waves* **11**, 447 (2002).
- [6] R. K. Linde and D. N. Schmidt, *J. Appl. Phys.* **37**, 3259 (1966).
- [7] R. R. Boade, *J. Appl. Phys.* **40**, 3781 (1969).
- [8] B. M. Butcher, *J. Appl. Phys.* **45**, 3864 (1974).
- [9] S. Bonnan, P. L. Hereil, and F. Collombet, *J. Appl. Phys.* **83**, 5741 (1998).
- [10] G. T. Gray III, N. K. Bourne and J. C. F. Milet, *J. Appl. Phys.* **94**, 6430 (2003).
- [11] A. D. Resnyansky, N. K. Bourne, *J. Appl. Phys.* **95**, 1760 (2004).
- [12] D. J. Pastine, M. Lombardi, A. Chatterjee and W. Tchen, *J. Appl. Phys.* **41**, 3144 (1970).
- [13] L. Boshoff-Mostert and H. J. Viljoen, *J. Appl. Phys.* **86**, 1245 (1999).
- [14] Q. Wu and F. Jing, *J. Appl. Phys. Lett.* **67**, 49 (1995).

- [15] Q. Wu and F. Jing, J. Appl. Phys. **80**, 4343 (1996).
- [16] H. Geng, Q. Wu, H. Tan, L. Cai and F. Jing, J. Appl. Phys. **92**, 5924 (2002).
- [17] P. Erhart, E. M. Bringa, M. Kumar, and K. Albe, Phys. Rev. B **72**, 052104 (2005).
- [18] Q. Yang, Guangcai Zhang, Aiguo Xu, Y. Zhao, Y. Li, Acta Phys. Sini. **57**, 940 (2008) (in Chinese).
- [19] F. H. Harlow, 1964 *Methods for Computational Physics*, Vol. **3**, 319-343, Adler B, Fernbach S, Rotenberg M (eds). Academic Press: New York .
- [20] D. Burgess, D. Sulsky, J. U. Brackbill, J. Comput. Phys. **103**, 1 (1992).
- [21] S. Bardenhagen, J. Brackbill, and D. Sulsky, Comput. Methods Appl. Mech. Eng. **187**, 529 (2000).
- [22] Y. J. Guo and J.A. Nairn, Computer Modeling in Engineering & Sciences **1**, 11 (2006).
- [23] N. P. Daphalapurkar, H Lu, D. Coker, R. Komanduri, Int. J. Fract. **143**, 79 (2007).
- [24] S. Ma, X. Zhang, X.M. Qiu, Int. J. Impact Eng. **36** 272 (2009).
- [25] Aiguo Xu, X F Pan, Guangcai Zhang and Jianshi Zhu, J. Phys.: Condens. Matter **19**, 326212(2007).
- [26] X. F. Pan, Aiguo Xu, Guangcai Zhang, et al, Commun. Theor. Phys. **49**, 1129 (2008).
- [27] X. F. Pan, Aiguo Xu, Guangcai Zhang and Jianshi Zhu, J. Phys. D: Appl. Phys. **41**, 015401 (2008).
- [28] H. Minkowski, Mathematische Annalen, **57** 447(1903).
- [29] H. Hadwiger, Abh. Math. Sem. Univ. Hamburg **20**, 136 (1956); Math. Z. **71**, 124 (1959).
- [30] D. H. Weinberg, J. R. Gott, A. L. Melott, Astrophys. J, **321**, 2 (1987).
- [31] A. L. Melott, Phys. Rep., **193**, 1 (1990).
- [32] K. R. Mecke, Phys. Rev. E **53**, 4794 (1996).
- [33] S. Winitzki and A. Kosowsky, arXiv: astro-ph/9710164v1.
- [34] A. Aksimentiev, K. Moorthi, R. Holyst, J. Chem. Phys. **112**, 1 (2000).
- [35] K. R. Mecke and V. Sofonea, Phys. Rev. E **56**, R3761 (1997).
- [36] Aiguo Xu, G. Gonnella and A. Lamura, Phys. Rev. E **67**, 056105(2003); Phys. Rev. E **74**, 011505(2006); Physica A **331**, 10 (2004); Physica A **344**, 750 (2004); Physica A **362**, 42 (2006); Aiguo Xu, G. Gonnella, A. Lamura, G. Amati and F. Massaioli, Europhys. Lett., **71**, 651 (2005).
- [37] W. T. Gózdź and R. Holyst, Phys. Rev. E **54**, 5012 (1996); Phys. Rev. Lett. **76**, 2726 (1996).
- [38] F. Auricchio, L. B. da Veiga, Int. J. Numer. Meth. Engng **56** 1375 (2003).
- [39] B. Zhang, et al. *Explosion physics*, Ordance Industry Press of China, 1997 Beijing.

This figure "Fig3.jpg" is available in "jpg" format from:

<http://arxiv.org/ps/0904.0130v1>

This figure "Fig7.jpg" is available in "jpg" format from:

<http://arxiv.org/ps/0904.0130v1>